Nuclear Instruments and Methods in Physics Research B 542 (2023) 188–194

Contents lists available at ScienceDirect

Nuclear Inst. and Methods in Physics Research, B

journal homepage: www.elsevier.com/locate/nimb

Energy loss profile measurements using the ACTAR TPC demonstrator active target

A. Camaiani [a,b], S. Barlini [a,b,*], A.A. Stefanini [a,b], G. Casini [b], H. Alvarez-Pol [c], A. Arokiaraj [d], L. Baldesi [a,b], R. Bolzonella [e,f], G. Cardella [g], C. Ciampi [h], M. Cicerchia [f,i], M. Cinausero [e], G. Collazuol [i], E. De Filippo [g], L. Domenichetti [e,f], D. Fabris [i], B. Fernández-Domínguez [c], E. Fioretto [e], C. Frosin [a,b], F. Galtarossa [i], J. Giovinazzo [l], B. Gnoffo [k,g], F. Gramegna [e], G.F. Grinyer [m], I. Lombardo [g], T. Marchi [e], N.S. Martorana [k,g], A. Mentana [d], P. Ottanelli [a,b], E.V. Pagano [j], J. Pancin [h], M.G. Pellegriti [g], S. Piantelli [b], S. Pirrone [g], O. Poleshchuk [d], R. Raabe [d], T. Roger [h], M. Russo [g], P. Russotto [j], L. Scomparin [e,f], J.A. Swartz [d,n], S. Valdré [b], G. Verde [g], M. Vigilante [o,p], J. Yang [d]

[a] Dipartimento di Fisica, Università di Firenze, I-50019 Sesto Fiorentino, Italy
[b] Istituto Nazionale di Fisica Nucleare, Sezione di Firenze, I-50019 Sesto Fiorentino, Italy
[c] IGFAE, Universídade de Santiago de Compostela, E-15782, Santiago de Compostela, Spain
[d] KU Leuven, Instituut voor Kern- en Stralingsfysica, 3001 Leuven, Belgium
[e] INFN Laboratori Nazionali di Legnaro, Viale Dell'Università 2, Legnaro (PD), Italy
[f] Università di Padova, Dipartimento di Fisica e Astronomia, Via Marzolo 8, Padova, Italy
[g] INFN - Sezione di Catania, Via S. Sofia, 64, 95123 Catania, Italy
[h] Grand Accélérateur National d'Ions Lourds (GANIL), CEA/DRF-CNRS/IN2P3, Bd. Henri Becquerel, 14076 Caen, France
[i] INFN - Sezione di Padova, Via Marzolo 8, Padova, Italy
[j] INFN - Laboratori Nazionali del Sud, via S. Sofia 62, 95123 Catania, Italy
[k] Dipartimento di Fisica e Astronomia "Ettore Majorana", Università degli Studi di Catania, Italy
[l] Centre d'Études Nucléaires de Bordeaux Gradignan, Université de Bordeaux—UMR 5797 CNRS/IN2P3, Chemin du Solarium, 33175 Gradignan, France
[m] Department of Physics, University of Regina, Saskatchewan S4S 0A2, Canada
[n] Department of Physics and Astronomy, Aarhus University, 8000, Aarhus C, Denmark
[o] Università degli Studi di Napoli Federico II - Corso Umberto I 40, 80138, Napoli, Italy
[p] INFN - Sezione di Napoli, via Cintia, 80126, Napoli, Italy

ARTICLE INFO

MSC:
00-01
99-00

Keywords:
Active target
TPC
Energy loss profile

ABSTRACT

The energy loss profiles of different ion beams (^{6}Li, ^{27}Al and ^{50}Ti) impinging on CF_4, isobutane and P10 have been measured with the active target ACTAR TPC demonstrator. The pressure of the gas, monitored during the experiment, has been chosen in order to stop the ions inside the active zone. Starting from the energy loss calculation produced by the SRIM code, the experimental ion tracks have been simulated, taking into account the effect of the thermal diffusion of electrons during their drift towards the pad plane under the effect of a uniform electric field. The uncertainty in the geometry, mainly due to the thickness and deformation of the mylar interface window between the gas volume and the high vacuum line, has been taken into account. A good agreement is obtained between the experimental and simulated energy loss profiles.

1. Introduction

A time projection chamber (TPC) used in Active Target mode is a modern device to perform peripheral reactions in inverse kinematics with radioactive ion beams (see [1], and references therein, for a recent review), where high detection efficiency and a thick target are necessary to compensate the weak beam intensity (~10^5 pps or lower). Moreover, since the reaction occurs within the same detection gas volume, a gaseous Active Target (in the following we will refer to it simply as Active Target, AT) allows to cover, with typical resolution $\Delta\theta \approx 1°$, a wide range of the light-ejectile scattering angles, even those usually not accessible in solid target experiments. In the last ten years, favored by the construction and/or upgrade of radioactive

* Correspondence to: Dipartimento di Fisica, Univerisità degli Studi di Firenze e INFN-Firenze, Via Giovanni Sansone 6 Sesto Fiorentino, 50019, FI, Italy.
E-mail address: barlini@fi.infn.it (S. Barlini).

https://doi.org/10.1016/j.nimb.2023.07.001
Received 17 April 2023; Received in revised form 5 June 2023; Accepted 1 July 2023
Available online 16 July 2023

ion beam facilities such as FRIB [2], SPIRAL [3], HIE-ISOLDE [4], FRAISE [5], SPES [6], as well as by detector technological advances, a new generation of AT has been developed (see [7,8] for exhaustive reviews). Some examples are ACTAR-TPC [9] at GANIL (France), Tex-AT [10] at Texas A&M (USA) and CAT [11] at HIMAC (Japan). In some cases they can be placed inside a magnet to further disentangle the kinematics variables, as in the case of AT-TPC [12] at NSCL/FRIB (USA), SpecMAT [13] at ISOLDE (CERN), or the SπRIT TPC [14] at RIKEN (JP).

As a key-point, an AT allows to reconstruct, event-by-event, the 3D view of the reaction tracks, thus accessing the reaction vertex and consequently the interaction energy (namely, the kinetic energy of the projectile at the vertex position). However, the interaction energy measurement needs to rely on the energy loss tables, also keeping into account the interface window between the gas volume and the high vacuum line, and some (possible) gas dead layers located in between the entrance window and the active region. For example, in the ACTAR TPC demonstrator [15], the detection setup used in this work, the entrance window consists of a mylar foil followed by approximately 60 mm of inactive gas. In addition, also the energy of the reaction products, stopped inside the active volume, can be inferred from energy loss calculation, directly measuring the range or from the shape of the track profile (namely the Bragg profile). Therefore, the energy loss tables are a key ingredient during an AT analysis. In this paper, we directly measure the Bragg profile of mono-energetic ions. Starting from such a profile, the stopping-power curve (dE/dx *vs* E) will be built, tracking the incoming ion along its whole path until it stops inside the active volume. The results will then be compared with the calculation of one of the most commonly used tool in nuclear physics: the SRIM program [16].

The SRIM program is a software package which calculates the Stopping and Range of Ions in Matter; in its MonteCarlo version (*i.e.* TRIM), it simulates the passage of an ion through different layers, keeping into account both electronic and nuclear stopping power, as well as energy and angular straggling effects. In this sense, the comparison of a simulation performed with this program with experimental data coming from an AT can be a direct test of the goodness of the energy loss tables, tracking the incoming ion well beyond the Bragg peak until it stops inside the active volume. As a matter of fact, in literature there are many examples of energy loss measurement (see the IAEA database on electronic stopping power [17] for the state of the art of experimentally available measurements). It is worth mentioning measurements performed in back scattering configuration that allow to explore low energy per nucleon on the projectile of interest (below 100 keV/nucleon) [18]. However, such measurements are mainly performed in transmission experiments (i.e. the impinging ion is punching-through the material of interest), while experimental measurements where the ion is stopped inside the active volume are, to our knowledge, quite scarce [19–21]. In this respect, an AT allows the direct reconstruction of a Bragg profile, following the slowing down of an ion inside the active volume: for example in [19] the Bragg profile of an alpha particle inside isobutane has been reconstructed, exploiting a triple alpha source (5.15 −5.48 - 5.8 MeV). The experimental results have been then compared with the, GEANT4 based, ACTAR-Sim code [22]. In ACTAR-Sim, the GEANT4 toolkit is used for the set-up description, primary ionization generation and particle tracking, while an additional ROOT [23] based program is used for the electron drift and multiplication to mimic the pad response.

Following these ideas, in this paper we report on experimental measurements on ^{6}Li, using the ACTAR TPC demonstrator [15] as a detection device filled with CF_4, isobutane and P10 (*i.e.* Ar+(10%)CH_4). Moreover, the energy loss profiles of ^{27}Al and ^{50}Ti in CF_4 are also measured. According to the literature [17], to date, no direct measurements for such ion-gas combinations are available. In particular, for Li ions the lowest experimentally measured energies on elements or molecules of interest are: 2 keV on solid C [24], 15 keV on CH_4 [25], 10–15 keV in H_2 [26,27] and 10 keV in Ar [26]. For Al and Ti ions only measurements on solid C are available, at minimum energies of 80 keV [28] and 250 keV [29]. In this work, for each dataset, the gas pressure of the AT has been chosen in order to stop the incoming ion within the active volume, thus accessing the energy loss up to the ion stopping region. This will allow us for achieving unprecedented stopping power regions for the aforementioned particles, up to the end of their tracks, and also measuring their range which will be then directly compared with the SRIM estimations. The layout of the paper is the following. Section 2 describes the experimental set-up, the beam-gas combinations, and the experimental data analysis. Section 3 discusses the original SRIM calculations and their tuning to fit the ACTAR TPC demonstrator geometry. In Section 4, the qualitative and quantitative comparison between experimental and simulated results is shown. Finally, the conclusions are presented in Section 5.

2. The detector and the experimental approach

The measurements were performed at the Laboratori Nazionali del Sud at Catania (Italy) using different ion beams accelerated by the TANDEM MP facility. In particular, a ^{6}Li beam at 9 MeV, a ^{27}Al beam at 75 MeV and ^{50}Ti beam at 142 MeV have been used with intensities reduced down to 10^2–10^3 pps in order to enter the ACTAR TPC demonstrator with negligible effects on spatial charge accumulation [30]. The active target was filled with different gases, namely CF_4, isobutane and P10, with gas pressures between 50 and 180 mbar. In this setup, the gas volume is separated from the high-vacuum beam line by a mylar foil, with a nominal thickness of 6 μm and a diameter of 1 cm.

A full description of the setup can be found in [15], here we recall only the main features. The detector is contained inside an Aluminum box, whose central volume is 300 × 250 × 210 mm^3, into which the gas is continuously flows to avoid gas aging (typical flow values are 2–3 times the gas volume per hour). The core of this demonstrator is the double field cage shown in Fig. 1 with two wire layers, namely the internal one and the external one, separated by a 10 mm gap. The wire diameter is 20 μm and the wire spacing is 1 mm for the internal cage and 5 mm for the external one, guaranteeing optical transparency of nearly 98%. Once the electrons arrive at the bottom electrode driven by the electric drift field, their amplification is performed using a MicroMegas [31] system consisting of a 45/18 stainless-steel woven micromesh and a PCB glued on an Al flange. The amplification gap, where the avalanche multiplication takes place, is approximately 220 μm. The homogeneity of such a gap has been measured in [15] using a collimated ^{55}Fe source mounted on an automated 2-dimensional scanning table: it results within ±1% in the whole pad plane. In this experiment, the reduced electric field within the MicroMegas is around 1.5 ·10^2 V/(cm mbar).

The pad plane visible in Fig. 1 is segmented in 64 × 32 pixels of 2 × 2 mm^2, including 40 μm of dead area all around the squared pixel. Each pad is connected to a channel of the GET electronics [32] (General Electronics for TPCs). The electronic system consists of a custom-designed ASIC (named AGET) for signal processing of 64 channels able to digitize the data through a 12-bits ADC. The ASIC chips are grouped into front-end cards (named ASAD) each housing 4 chips. A concentration board (CoBo) hosted into a MicroTCA crate can read and process the digital data from up to 16 ASICs (4 complete ASAD). The system is modular and it can handle up to 33792 channels. A trigger module (MuTanT) completes the system, while data can be acquired using an ethernet connection to the MicroTCA crate. The system is fully programmable in terms of electronics gain and threshold for each channel and trigger setup.

To perform a clean comparison between measured energy loss profiles and simulated ones (see next section), a key ingredient is the thickness of the dead layers crossed by the incoming ion before reaching the sensitive region, *i.e.* the mylar window thickness and the gas volume upstream from the active one. The inert gas length has

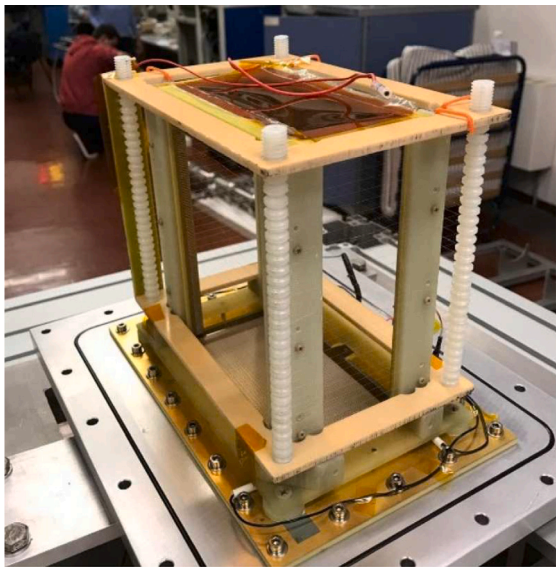

Fig. 1. The double field cage of the ACTAR TPC demonstrator apparatus. On the bottom, the pad plane consists of 64 × 32 pixels, each 2 × 2 mm^2 wide.

been measured to be 58 ± 1 mm. Concerning the mylar thickness, the nominal value is 6 μm, as declared by the producer and confirmed (with an uncertainty of ±0.5 μm) by a specific energy loss measurement performed with a ^{241}Am alpha particle source. Moreover, here we take into account another effect which can have an impact on the energy loss measurement: the deformation induced by the pressure difference between the gas chamber and the beam line during the measurements. Since the entrance window has a circular opening of 1 cm diameter, we are interested in evaluating how much this flat surface is deformed. After several tests, we estimated that the planar mylar surface transforms under pressure into a spherical cap with a sagitta of 2 ± 1 mm. Since the mylar is glued all around the borders of the entrance hole, one must consider the effect of the stretching on the effective thickness in measurement conditions. By simple geometrical arguments, one can consider that the mylar thickness has decreased as the ratio between the surface before and after the deformation. In this approximation, the estimate of the effective thickness is 5.2 ± 0.7 μm, where in the error we also included the initial uncertainty on the foil thickness.

A preliminary procedure of equalization of the MicroMegas electronic gain for each output channel is necessary. This has been obtained by means of a pulser run, where the pulser signal has been injected directly into the mesh layer: in this way, the same total charge deposited into the pads will correspond to the same signal amplitude at the end of the electronics chain, irrespective of the pads involved. A typical good track detected in AT in the case of ^{6}Li at 9 MeV impinging on CF_4 is shown in Fig. 2 panel a), with the 3D reconstruction drawn on top while the projection on the pad plane is shown on the bottom. We remind that, due to the low beam intensity, only one track is detected per event,[1] thus a clusterization procedure, which could introduce a perturbation in the Bragg profile reconstruction, is not necessary. Nevertheless, a fraction of spurious events (less than 2% of the total) is still present. First of all, noisy events can occur since the thresholds on the pad signals are kept close to the limit of the noise. They are characterized by an anomalous number of fired pads, as one can see in Fig. 2 panel b) bottom. Moreover, there are seemingly good tracks but with directions not ascribable to the beam optics, as the one shown in Fig. 2 panel c). Usually, they are also characterized by a different total charge. Finally, there are rare nuclear reaction events occurring in the gas or in the mylar window. The spurious events are removed on the basis of geometrical arguments, number of fired pads and total deposited charge.

One of the critical points during our experiment is the stability of the pressure: this can be checked also directly by looking at the experimental data. Each combination of gas and beam corresponds to an experimental run, typically including 10^3–10^4 events. Looking at the total charge as a function of the event number, it is possible to point out variations in the gas pressure: the high stability and reproducibility of the beam energy (of about 10^{-3}) ensures that the total energy deposited into the gas is constant. Consequently, keeping in mind the presence of the inactive zone before the active one, a systematic increase of the pressure corresponds to a decrease of the energy loss in the active area, and vice versa. All the measured combinations of ion/gas, ^{6}Li at 9 MeV on three different gases (CF_4, isobutane and P10) and ^{27}Al at 75 MeV and ^{50}Ti at 142 MeV in CF_4, do not show systematic variations within the expected statistical fluctuations and the experimental resolution (which is 2%–3% considering the total charge distribution). The experimental energy loss profiles that will be shown in the following are not the results of a single ion beam interaction. They correspond to the average profiles obtained for each ion/gas combination run, as a matter of fact the relative statistical error on the stopping power for each depth bin is at the most 1% at the end of the track. Such profiles are going to be compared with the simulation results described in the following section.

3. The SRIM simulation

The SRIM [16] package has been chosen to compare the energy loss profile measured in the active gas zone with the model predictions. SRIM is based on the works of Ziegler et al. and it is updated by the authors. Within SRIM calculations, the entrance mylar window and the inactive gas layer of the experimental device have been included. As for the selected experimental tracks, we assume tracks entering the AT volume in parallel to the longitudinal axis, so we limit the simulations in 2D, as shown in Fig. 3 for one of the studied gas/ion combination. The impinging particles have always been considered to enter exactly at the middle of the lateral side of the pad plane. Starting from this distribution, a 2D histogram has been created, which corresponds to the distribution of the energy loss.

Before considering the discretization introduced by the granularity of the pad plane, placed 60 mm away from the detector entrance, it is necessary to take into account the effect of the thermal diffusion acting during the electron drift towards the anode, driven by the constant electric field which acts sharply in the simulated data from the beginning of the pad plane. This effect produces a 2D gaussian broadening of the spacial distribution of the primary electrons when they reach the pad plane [33]. For each ion–electron pair the centroid of the gaussian distribution is the same as their initial position, while the standard deviation (equal on both axes) follows the expression $\sigma_{drift} = \sqrt{2D_T h/v_{drift}}$, where D_T is the diffusion coefficient, v_{drift} is the electron drift velocity and finally h is the distance traveled by the electrons (h=10 cm in our case). The first two parameters depend on the gas and on the operation conditions (pressure, electric field, temperature...).

In Table 1, the values of the gas pressure p and the reduced electric field ϵ chosen in the experiment are shown together with the diffusion coefficient D_T, the drift velocity v_{drift} and the σ_{drift} applied to simulate the thermal diffusion obtained using the Magboltz code [34] in the case of ^{6}Li at 9 MeV impinging on the different gases used in the experiment, while in Table 2 the same values are shown for ^{27}Al at 75 MeV and ^{50}Ti at 142 MeV on CF_4. The distribution has been then discretized taking into account the pad plane geometry (2 × 2 mm^2), including

[1] Only in a negligible number of cases more than one track has been observed, corresponding to nuclear interactions between the beam and the gas nuclei.

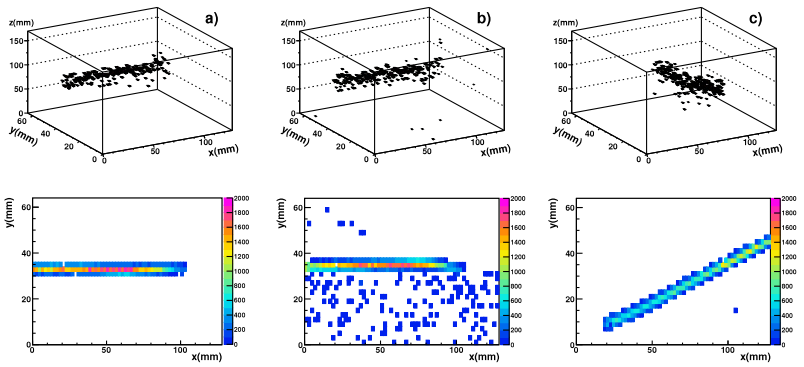

Fig. 2. 3D reconstructions (upper panels) and 2D projections on the pad planes of some events: panel a) is a typical event for a Li ion on CF_4 gas, panel b) is a noisy event while in panel c) a spurious track event is shown.

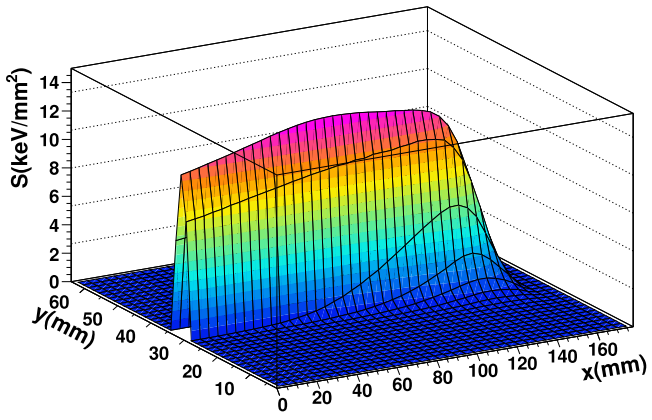

Fig. 3. The 2-D energy loss distribution of ^{6}Li at 9 MeV in 180.5 mbar of P10 as simulated by the SRIM [16] program.

Table 1
Values of the parameters (D_T, v_{drift} and σ_{drift}) evaluated with Magboltz for the ^{6}Li at 9 MeV beam energy impinging on different gases.

^{6}Li in	p (mbar)	ϵ (V/cm)	D_T (cm^2/s)	v_{drift} (cm/ns)	σ_{drift} (cm)
CF_4	69.6	100	4875	0.0113	0.093
Isobutane	55.0	100	5743	0.0045	0.160
P10	180.5	52.9	43760	0.0045	0.441

Table 2
Values of the parameters (D_T, v_{drift} and σ_{drift}) evaluated with Magboltz for the CF_4 gas for ^{27}Al and ^{50}Ti runs.

ion in CF_4	p (mbar)	ϵ (V/cm)	D_T (cm^2/s)	v_{drift} (cm/ns)	σ_{drift} (cm)
^{27}Al	101.0	75	4606	0.00960	0.098
^{50}Ti	90.0	67.5	4850	0.00962	0.100

the 40 μm dead frame around each pad. Finally, the same detection threshold is applied to each pad to reproduce the experimental energy detection thresholds. In the following, in Fig. 4, we briefly describe the adopted simulation steps, using the Li ions impinging on P10 as a representative case, where the effect of the transverse diffusion is larger. Starting from the stopping power generated by SRIM averaged on 10^4 different events (3D view in Fig. 3), the initial x-y distribution is created (panel a), then the energy loss is spread following a gaussian distribution in order to take into account the thermal diffusion of the primary electrons towards their motion to the pad plane (panel b)). Eventually, the discretization effect (as well the dead area of each pad) is introduced (panel c)), generating a final picture of the pad plane which can now be compared to the experimental distribution of all the selected events (panel d)). From a qualitative point of view, the final simulated distribution is in good agreement with the experimental one, thus validating our procedure. Comparing the average energy loss profile at each simulation step, the effects of the thermal diffusion and of the energy detection threshold can be highlighted separately. This is shown in Fig. 5 for the case of Li ions on P10: the original energy loss profile produced by SRIM is drawn with black points, while magenta points represent the energy loss profile once the thermal diffusion and the granularity of the pad plane (including the dead frame) are considered. Eventually, the effects introduced by the energy detection threshold are reported as blue open dots. The thermal diffusion affects the Bragg curve mainly in the Bragg peak region, at the end of the profile, as one can see in the inset of Fig. 5. On the other side, the energy detection threshold effect is practically negligible. In conclusion, the main effect through the various steps is associated with the decrease in the total energy loss due to the pad dead frame (8% in case of complete insensitivity of the dead area, but irrelevant to the final goal of this work).

4. Comparison between experimental data and simulation

In order to perform a clean direct comparison between experimental data and simulations the corresponding distributions are reported in the following, neglecting the data collected from the first two rows of the pad plane ($x < 4$ mm), since the assumption of a sharp inset of the constant electric field may be questionable. The comparison is shown in Fig. 6 for the ^{6}Li at 9 MeV impinging on CF_4, isobutane and P10. Fig. 7 shows the comparison for ^{6}Li at 9 MeV, ^{27}Al at 75 MeV and ^{50}Ti at 142 MeV on CF_4. For the sake of clarity, the ^{6}Li at 9 MeV on CF_4 is repeated at the top panel of the two pictures. In both cases, the red points correspond to the experimental energy loss profile, while the simulated ones are drawn as a blue confidence zone, determined by the uncertainties in the values of the dead thicknesses before the active zone. The experimental distributions are normalized to the integral of the center of the confidence simulated zone. Each experimental point refers to the center of the pad along the x-direction (2 mm pitch) with an error on the stopping power due to the uncertainty in the normalization factor, which includes both the experimental total charge resolution and the systematical error on the simulation. Keeping into account the aforementioned deformation of the entrance window, the confidence region on the simulated profile takes into account the uncertainty on the mylar window thickness (5.2 ±0.7 μm) and on the dead gas layer depth (60 ± 2 mm). It has been built considering the simulated energy loss profile which is obtained using the minimum (4.5 μm) and the maximum (5.9 μm) entrance mylar thickness, varying consequently the gas dead layer.

The results of Fig. 6 permit the comparison of the same ion (^{6}Li at 9 MeV) in different gases, while those in Fig. 7 refer to different ions (from Z=3 up to Z=22) in the same gas. In all cases the shape agreement

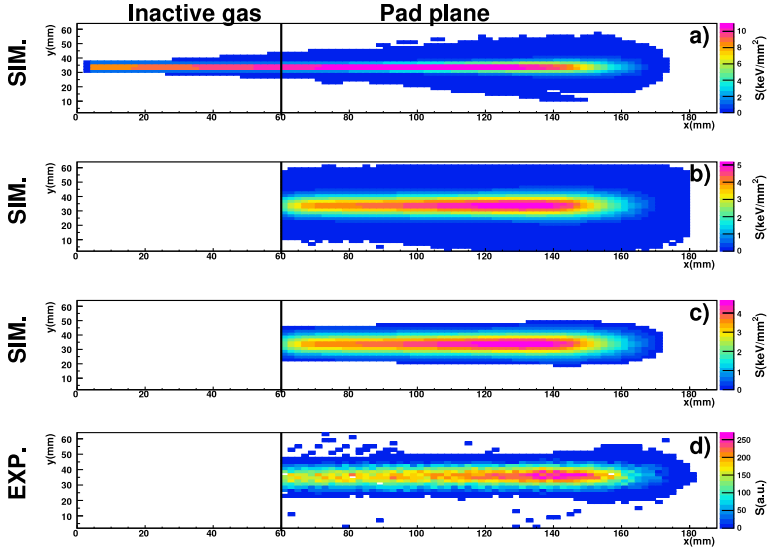

Fig. 4. The effect of the thermal diffusion in the simulation in the case of ^{6}Li at 9 MeV in 180.5 mbar of P10. Panel a): the 2-D histogram built starting from the energy loss profile produced by SRIM (z-axis expressed in keV/mm^2). Panel b): the 2D histogram after the thermal diffusion at the level of the pad plane. Panel c): the final distribution considering the $2 \times 2\,\mathrm{mm}^2$ pixel surrounded by 40 μm dead area and including an energy threshold to simulate the zero-suppression present in the GET electronics. Panel d): the experimental distribution corresponding to all the events (z-axis in arbitrary units).

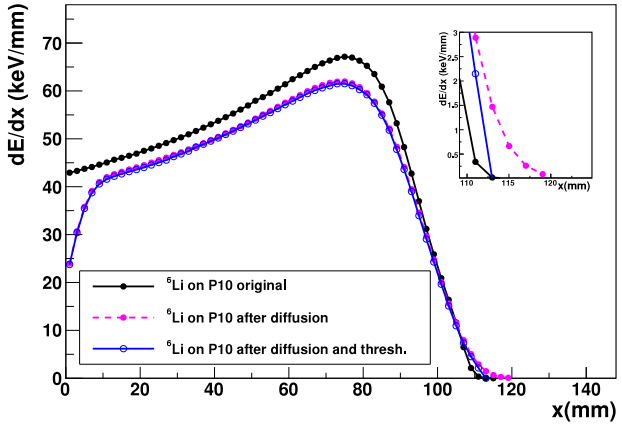

Fig. 5. Energy loss profile of ^{6}Li at 9 MeV in 180.5 mbar of P10: black points represent the original profile calculated using SRIM. Magenta points: energy loss profile after the thermal diffusion and the dead zone of 40 μm all around the pixels (mainly visible only in the inset). Finally, the blue open dots include the energy threshold too.

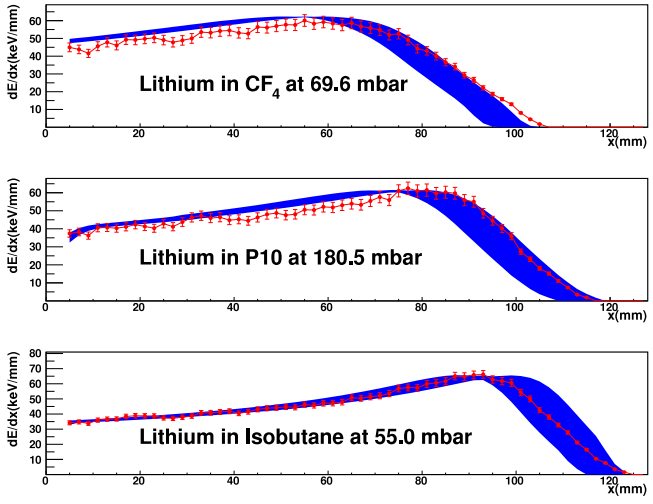

Fig. 6. Energy loss profile comparison between experimental data (red points) and simulation (blue) for ^{6}Li at 9 MeV impinging on CF_4 (top panel), P10 (middle panel) and isobutane (bottom panel). Each point refers to the center of the pad (2 mm pitch) along the x-direction. Lines are drawn to guide the eye.

between calculations and experimental results is satisfying, especially for Li in isobutane. The Al and Ti energy loss profiles of Fig. 7 are very interesting because they are the heavier ions tested in our experiment: in the case of Al the simulation well mimics the experimental data, while for the Ti a significant difference appears at the end of the energy loss profile, where the effects due to the change of the average charge ion state could affect the comparison more. A quantitative comparison summary using as estimators the depths in the active zone at different fractions of the maximum energy loss, namely the 50 % (half maximum depth HMD) as performed also in [19] and the 10% (tenth maximum depth TMD), is shown in Table 3 for ^{6}Li at 9 MeV in different gases and Table 4 for different ions in CF_4. The relative error attributed to the experimental values is obtained looking at the distribution of the depth profiles built event by event (about 2%–3% depending on the case), while in the simulated depth we consider the width of the confidence zone.

In Tables 3 and 4, also the results from the original SRIM energy loss profiles are reported. It is worth mentioning that both the HMD and TMD estimators are not affected by the proposed procedure to simulate the electron drift and the charge collection.

The agreement on both HMD and TMD between ^{6}Li values in various gases is excellent for the isobutane case (within 2%) and it worsens in the CF_4 and P10 cases (within 7% and 4%, respectively), but still consistent with the simulation uncertainty (see 3).

The simulated HMD and TMD for ^{27}Al in CF_4 are consistent with the experimental ones within the error bars. For the Ti case, as already suggested by the Bragg profile comparison (Fig. 7), both calculated range estimators deviates outside the uncertainties of 8% and 12% (HMD and TMD, respectively).

The experimental and simulated Bragg profiles can be transformed in stopping power curves by deconvoluting for the experimental effects and then by integrating the Bragg profiles starting from their ending side. The results are shown in Fig. 8 and in Fig. 9, allowing for an

Table 3
Depth in the active gas at 50% (HMD) and 10% (TMD) fraction of energy loss maximum for ^{6}Li at 9 MeV impinging on different gases for experimental and simulated data with or without the proposed procedure to consider the electron drift and the charge collection.

^{6}Li in	Exp. HMD (mm)	Sim. HMD (mm)	Orig. HMD (mm)	Exp. TMD (mm)	Sim. TMD (mm)	Orig. TMD (mm)
CF_4	89 ± 2	83 ± 5	83 ± 4	102 ± 3	95 ± 5	95 ± 4
P10	100 ± 2	96 ± 5	96 ± 4	112 ± 2	108 ± 5	107 ± 4
Isobutane	109 ± 3	108 ± 6	108 ± 5	119 ± 3	117 ± 5	117 ± 5

Table 4
Depth in the active gas at 50% (HMD) and 10% (TMD) fraction of energy loss maximum for ^{6}Li, ^{27}Al and ^{50}Ti impinging on CF_4 for experimental and simulated data with or without the proposed procedure to consider the electron drift and the charge collection.

	Exp. HMD (mm)	Sim. HMD (mm)	Orig. HMD (mm)	Exp. TMD (mm)	Sim. TMD (mm)	Orig. TMD (mm)
^{6}Li	89 ± 2	83 ± 5	83 ± 4	102 ± 3	95 ± 5	95 ± 4
^{27}Al	64 ± 2	65 ± 3	65 ± 2	85 ± 2	82 ± 5	82 ± 3
^{50}Ti	82 ± 2	75 ± 3	75 ± 3	115 ± 3	101 ± 4	101 ± 3

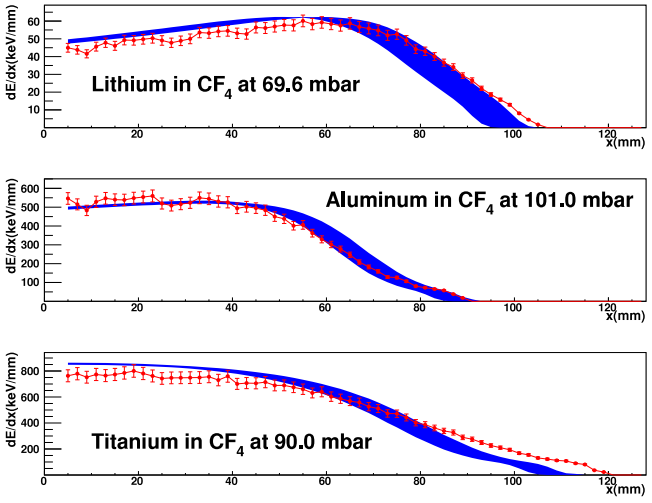

Fig. 7. Energy loss profile comparison between experimental data (red points) and simulation (blue) for ^{6}Li at 9 MeV (top panel, the same as previous picture), ^{27}Al at 75 MeV (middle panel) and ^{50}Ti at 142 MeV (bottom panel) impinging on CF_4. Each point refers to the center of the pad (2 mm pitch) along the x-direction. Lines are drawn to guide the eye.

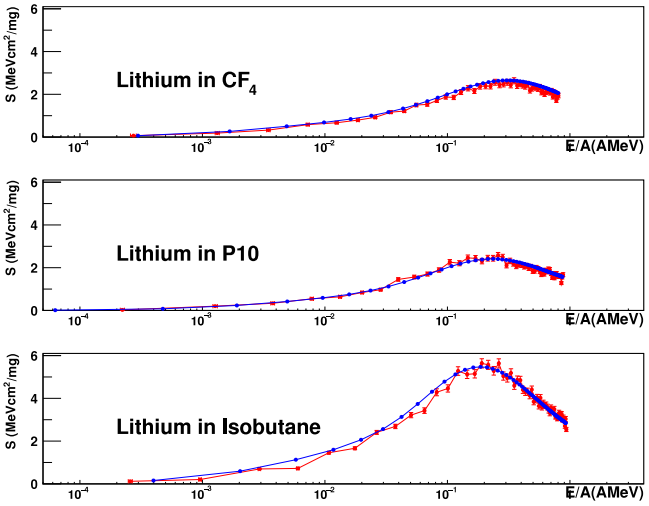

Fig. 8. Stopping power comparison between experimental data (red points) and simulation (blue) for ^{6}Li at 9 MeV impinging on CF_4 (top panel), P10 (middle panel) and isobutane (bottom panel). Lines are drawn to guide the eye.

overall comparison between experimental data and simulation in a wide ion energy range from less than 1 keV/nucleon to 1 MeV/nucleon.

As expected, we confirm the main results discussed about the previous pictures: the agreement between experimental data and SRIM simulation is in general good, as particularly evident in the case of Lithium in isobutane and P10. The Lithium and Aluminum in CF_4 are slightly worse, but still compatible considering the error bars, while Titanium in CF_4 presents the highest difference and the simulated data systematically exceed the experimental curve.

5. Conclusions

Bragg curves and energy loss distributions of different combinations of ion beams at MeV energies and gases have been directly measured using the ACTAR TPC demonstrator. In particular, we have measured the energy loss of a ^{6}Li beam at 9 MeV in different gases (CF_4, P10 and isobutane) and three ion beams (^{6}Li at 9 MeV, ^{27}Al at 75 MeV and ^{50}Ti at 142 MeV) absorbed in the same gas (CF_4). The gas pressure has been chosen in order to properly stop the beams well inside the gas volume. The use of this detector permits for the direct measurement of the Bragg curve, which can be compared with calculated energy loss profiles. Spurious event tracks have been removed before obtaining

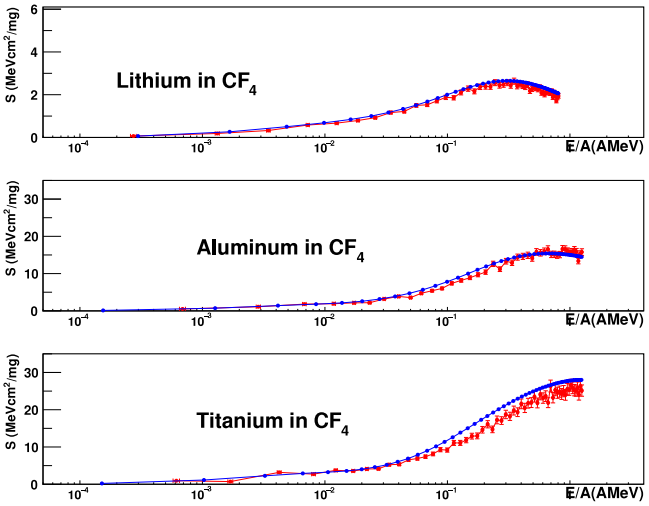

Fig. 9. Stopping power comparison between experimental data (red points) and simulation (blue) for ^{6}Li at 9 MeV (top panel, the same as previous picture), ^{27}Al at 75 MeV (middle panel) and ^{50}Ti at 142 MeV (bottom panel) impinging on CF_4. Lines are drawn to guide the eye.

energy loss profiles averaged over the number of tracks collected for each run.

The measured profiles have been compared to those calculated through the SRIM MonteCarlo code: taking into account the entrance window foil (with its deformation under operation) and the initial gas dead region before the active volume, the simulated energy loss profiles are then filtered introducing a correction for the electron diffusion along the drift path to the pad plane and including the real pixel granularity and geometry of the MicroMegas layer. The effect of the acquisition threshold has finally been considered.

Two estimators (HMD, half maximum depth, and TMD, tenth maximum dept) have been introduced for the quantitative comparison between experimental and simulated data. The apparatus filter applied to the original SRIM simulations to reproduce various experimental effects resulted to be of weak influence on the energy loss profiles: there are marginal modifications in the tails and around the Bragg's peak, but basically no effects on the proposed profile shape estimators. The agreement between simulated and experimental estimators is within the uncertainties for the Li ions on the three measured gases; same conclusions can be drawn for Al on CF_4, while Ti on CF_4 presents deviations outside the errors.

In this paper we have shown that a modern active gas detector, planned to investigate nuclear physics cases via nuclear reactions, represents also a good device for studies of ion energy loss in gases, also accessing energies below the typical values achievable with the usual transmission technique. In the ion/gas combinations studied in this work, the minimum measured energies are below 10 keV.

CRediT authorship contribution statement

A. Camaiani: Data analysis, Writing – original draft. **S. Barlini:** Data taking, Data analysis, Simulation, Writing – original draft. **A.A. Stefanini:** Data analysis, Simulation, Writing – original draft. **G. Casini:** Data taking, Supervision,Writing – review & editing. **H. Alvarez-Pol:** Writing – review & editing. **A. Arokiaraj:** Data taking, Writing – review & editing. **L. Baldesi:** Writing – review & editing. **R. Bolzonella:** Data taking, Writing – review & editing. **G. Cardella:** Data taking, Writing – review & editing. **C. Ciampi:** Writing – review & editing. **M. Cicerchia:** Data taking, Writing – review & editing. **M. Cinausero:** Writing – review & editing. **G. Collazuol:** Writing – review & editing. **E. De Filippo:** Data taking, Writing – review & editing. **L. Domenichetti:** Data taking, Writing – review & editing. **D. Fabris:** Writing – review & editing. **B. Fernández-Domínguez:** Writing – review & editing. **E. Fioretto:** Writing – review & editing. **C. Frosin:** Writing – review & editing. **F. Galtarossa:** Writing – review & editing. **J. Giovinazzo:** Writing – review & editing. **B. Gnoffo:** Data taking, Writing – review & editing. **F. Gramegna:** Writing – review & editing. **G.F. Grinyer:** Writing – review & editing. **I. Lombardo:** Data taking, Writing – review & editing. **T. Marchi:** Conceptualization, Data taking, WWriting – review & editing. **N.S. Martorana:** Data taking, Writing – review & editing. **A. Mentana:** Data taking, Writing – review & editing. **P. Ottanelli:** Writing – review & editing. **E.V. Pagano:** Data taking, Writing – review & editing. **J. Pancin:** Writing – review & editing. **M.G. Pellegriti:** Data taking, Writing – review & editing. **S. Piantelli:** Writing – review & editing. **S. Pirrone:** Data taking, Writing – review & editing. **O. Poleshchuk:** Data taking, Writing – review & editing. **R. Raabe:** Writing – review & editing. **T. Roger:** Data taking, Writing – review & editing. **M. Russo:** Writing – review & editing. **P. Russotto:** Data taking, Writing – review & editing. **L. Scomparin:** Data taking, Software,Writing – review & editing. **J.A. Swartz:** Data taking, Writing – review & editing. **S. Valdré:** Writing – review & editing. **G. Verde:** Data taking, Writing – review & editing. **M. Vigilante:** Data taking, Writing – review & editing. **J. Yang:** Data taking, Writing – review & editing.

Declaration of competing interest

The authors declare that they have no known competing financial interests or personal relationships that could have appeared to influence the work reported in this paper.

Data availability

Data will be made available on request.

Acknowledgments

We warmly thank GANIL Laboratories for making available the ACTAR Demonstrator. We acknowledge gratefully M. D'Andrea (INFN-CT) for the design of the lateral silicon-wall flange of the ACTAR TPC demonstrator and for its continuous help during the mounting and data taking phases, and G. Saccà (INFN-CT) for the use of the Dual Gain boards. We are also indebted to S. Salamone, D. Rizzo, G. Pastore, C. Marchetta and A. Massara (INFN-LNS) for their help in the mounting of the apparatus. We thank the Accelerator and Technical Division, the Electronic Service and the Data Acquisition Service of the INFN-LNS for their fundamental support in the mounting of the apparatus and the excellent beam quality. This project has received funding from the European Union's Horizon 2020 research and innovation programme under the Marie Skłodowska-Curie grant agreement FiBRa - No 101025651.

References

[1] D. Bazin, et al., Prog. Part. Nucl. Phys. 114 (2020) 103790.
[2] FRIB - https://frib.msu.edu/.
[3] GANIL-SPIRAL2 - https://www.ganil-spiral2.eu/.
[4] ISOLDE - https://isolde.cern/.
[5] FRAISE - https://potlns.lns.infn.it/it/motivazioni-scientifiche/fraise.html.
[6] SPES - https://web.infn.it/spes/.
[7] Y. Ayyad, et al., Eur. Phys. J. A (2018) 181.
[8] S. Beceiro-Novo, et al., Prog. Part. Nucl. Phys. 84 (2015) 124–165.
[9] B. Mauss, et al., Nucl. Instrum. Meth. A 940 (2019) 498.
[10] E. Koshchiy, et al., Nucl. Instrum. Meth. A 957 (2020) 163398.
[11] S. Ota, et al., J. Radioanal. Nucl. Chem. 305 (2015) 907.
[12] J. Bradt, et al., Nucl. Instrum. Meth. A 875 (2017) 65.
[13] O. Poleshchuk, et al., Nucl. Instr. Meth. A 1015 (2021) 165765.
[14] R. Shane, et al., Nucl Instr. Meth. A 784 (2015) 513–517.
[15] T. Roger, et al., Nucl. Instrum. Meth. A 895 (2018) 126.
[16] J.F. Ziegler, et al., Nucl. Instr. Meth. B 268 (2010) 1818, See www.SRIM.org for more information.
[17] IAEA - https://www-nds.iaea.org/stopping/index.htmljl.
[18] M.A. Sortica, et al., Phys. Rev. A 96 (2017) 032703.
[19] P. Konczykowski, et al., Nucl. Instrum. Meth. A 927 (2019) 125.
[20] M. Barbui, et al., Nucl. Instrum. Method B 268 (2010) 20–27.
[21] J.E. Johnstone, et al., Nucl. Instrum. Method A 1014 (2021) 165697.
[22] ACTAR.SIM - https://github.com/ActarSimGroup/Actarsim.
[23] ROOT - https://root.cern.
[24] J.H. Ormrod, H.E. Duckworth, Can. J. Phys. 41 (1963) 1424.
[25] Y.A. Teplova, V.S. Nikolaev, I.S. Dmitriev, L.N. Fateeva, Sov. Phys. -JETP 15 (1962) 31.
[26] H.H. Andersen, F. Besenbacher, H. Knudsen, Nucl. Instrum. Methods Phys. Res. 149 (1978) 121.
[27] S.K. Allison, C.S. Littlejohn, Phys. Rev. 104 (1956) 959.
[28] B. Fastrup, P. Hvelplund, C.A. Sautter, K. Dansk, Videnskab. Selskab Mat.-Fys. Medd. 35 (10) (1966).
[29] P. Hvelplund, B. Fastrup, Phys. Rev. 165 (1968) 408.
[30] J.S. Randhawa, et al., Nucl. Inst. Meth. A 948 (2019) 162830.
[31] I. Giomataris, et al., Nucl. Instrum. Meth. A 560 (2006) 405.
[32] E.C. Pollacco, et al., Nucl. Instrum. Meth. A 887 (2018) 81.
[33] A. Peisert, F. Sauli, Cern –service d'information scientifique-, RD/638-2500-Juillet, 1984.
[34] S. Biagi, MAGBOLTZ, CERN program library, 2011.